Solar evaporation performance of 3D-printed concave structures filled with activated carbon under low convective flow

R. Fillet, Vincent Nicolas, Alain Celzard, Vanessa Fierro

Solar evaporation performance of 3D-printed concave structures filled with activated carbon under low convective flow

R. Fillet[1], V. Nicolas[1*], A. Celzard[1,2], V. Fierro[1*]

[1] Université de Lorraine, CNRS, IJL, F-88000 Epinal, France

[2] Institut Universitaire de France (IUF)

[*]**Corresponding Author**: vincent.nicolas@univ-lorraine.fr

[*]**Corresponding Author**: vanessa.fierro@univ-lorraine.fr

Abstract

Three-dimensional (3D) geometries were 3D-printed to make unique geometries filled with activated carbon to improve water transport and photothermal conversion when used as solar evaporators. Evaporation was modelled to study the different aspects affecting the evaporation performance of five geometries. Low convection airflow, concave surface evaporation, light reflection and natural convection were investigated in a 2D flat surface and four 3D structures presenting a concave surface. It was revealed that the effect of surface-to-surface radiation has a limited impact on the evaporation rate (1%), which depends linearly on the evaporation area. We have undoubtedly shown that, both in forced and natural convection, concavity in the structure should be avoided as it leads to moisture-saturated air. On the contrary, the 3D structure should be as open as possible to allow the unsaturated air to escape.

Keywords: Simulation; Biosourced materials; Solar evaporation; Heat and mass transfers; Activated Carbon

1 Introduction

Water is a basic human need, whether for drinking of domestic use. The World Health Organisation estimates that at least 100 L per person per day are needed to meet these needs. The recommended minimum water consumption is 5.3 L per person per day, with the rest used for cooking and hygiene [1]. Due to our growing population, river pollution and global warming, it is estimated that by 2050, 3.9 billion people, or more than 40% of the world's population, will be living in water-stressed areas [2]. It is therefore necessary to develop new solutions to produce clean water using less energy.

Solar energy is a promising energy to harness, as the amount that reaches the earth in one hour can cover the energy needs of mankind for a year [3]. As previously proven, solar energy is well suited to the production of clean water using an evaporation system [4] and show potential for cogeneration of steam and electricity [5].

Water evaporation is a phenomenon that occurs at the interface between water, whether liquid or adsorbed on a surface, and air. We have shown elsewhere that water evaporation depends on the temperature of the air around the evaporating material [6]. Humidity also plays a role, but to a lesser extent. Indeed, increasing the air temperature also increases the saturation vapour pressure, which allows the air to contain more water. In addition, increasing the interface temperature increases the local air temperature and allows more water to evaporate. The reader will draw a practical parallel by imagining that to dry clothes, it is better to hang them outside in the sun than to leave them to dry folded in a small room without ventilation. To achieve high evaporation performance, the material must be highly light absorbent and heat must be maintained at the interface [7,8]. Usually, an insulating foam is used to keep the heat at the surface, on which the material is positioned with light shining on it. Water is pumped either through the material or through cotton or another highly water

53 diffusing material. These materials can be made from metallic nanostructures, inorganic
54 semiconductor nanostructures, polymers or carbon [9].

55 Bio-based materials are excellent candidates for evaporative water production, as well as
56 easy to access and produce. Recently, using carbonised coffee grounds, Xiao et al. succeeded
57 in producing clean water at a rate of 1.49 kg m^{-2} h^{-1} under 1 sun (1 sun is equal to the standard
58 illumination of the earth, i.e., 1 kW m^{-2}) [10]. Using a polyethylene / graphene foam, Xie et
59 al. were able to evaporate at 1.83 kg m^{-2} h^{-1} [11] and Li et al. achieved 1.39 kg m^{-2} h^{-1} using a
60 polypyrrole-sorghum straw bilayer material [12], both under 1 sun illumination. Hydrogel is a
61 type of material that performs well, as shown by Li et al. who made a dual-region hydrogel
62 that produced 3.69 kg m^{-2} h^{-1} under 1 sun [13], and by Zhu et al. who used a chitosan / PVA
63 hydrogel that gave 2.28 kg $m^{-2}.h^{-1}$ and, with a 3D enhancement, up to 3.80 kg m^{-2} h^{-1} [14].

64 In addition, heat and mass transfer can be accelerated by forced convection. For example,
65 Wang et al. fabricated a spiral cellulose sponge that allowed water evaporation at 4.35 kg m^{-2}
66 h^{-1} under one sun illumination and a convective flow of 4 m s^{-1}, which is a 179%
67 improvement over natural convection [15]. Liu et al. obtained similar results using CNT-
68 coated corrugated paper, i.e., a water evaporation of 5.55 kg m^{-2} h^{-1} under 1 sun and a
69 convective flow of 5 m s^{-1}, which is a 232% improvement over natural convection [16].
70 Finally, Cheng et al. fabricated a hydrogel and tested it using convective flow under outdoor
71 conditions: water evaporation ranged between 1.5 and 3.5 kg m^{-2} h^{-1}, under 0.5 to 0.8 sun and
72 0.2 to 0.6 m s^{-1} wind speed [17]. Compared to previous studies [15,17,18], the airflow rate
73 was lower but allowed the wind speed to be exploited in an outdoor system. Furthermore, the
74 renewal of the air inside the structure could avoid the saturation that occurs in traditional
75 outdoor experiments, which and reduces evaporation [19].

76 Another way to increase performance is indeed to use 3D structures, which have more
77 surface area available for evaporation. Yu et al. thus fabricated a cellulose acetate filter

78 decorated with reduced graphene oxide and achieved 2.81 kg m^{-2} h^{-1} under 1 sun illumination
79 [20]. Ivan et al. recycled egg trays and toners to make a 3D evaporator that produced 1.3 kg
80 m^{-2} h^{-1} under 1 sun [21] and Li et al. made a laponite / silicon sponge that achieved 1.77 kg m^{-2} h^{-1}
81 under 1 sun [22]. Similarly, using *Juncus effusus* and activated carbon (AC) powder,
82 Zhang et al. were able to produce 2.23 kg m^{-2} h^{-1} of clean water under 1 sun illumination [23].

83 Carbon is a material of choice for solar evaporation applications, and various carbon
84 materials have been used for this purpose, such as carbonised biomass, carbon nanotubes,
85 graphene or AC [24]. AC absorbs around 95% of solar radiation [25], can transport water well
86 and has therefore been used to enhance the performance of other materials that are themselves
87 good water carriers, such as foams [26] or paper [27]. Besides the addition of AC, the
88 geometry of the evaporation system can improve solar evaporation [28–31] by reflecting the
89 radiation. Some of the radiation arriving on a concave surface is absorbed and some reemitted
90 and can be absorbed by another part of the concave surface, thus increasing the performance
91 as the material absorbs more energy. Using a 3D cylinder, which was supposed to harness the
92 power of surface-to-surface radiation, Shi et al. [29] obtained an average evaporation rate of
93 1.90 kg m^{-2} h^{-1}. Zhao et al. [28] used a conical hydrogel evaporator and achieved 2.64 kg m^{-2}
94 h^{-1}, Yang et. al. [30] used 3D printing to produce aerogel arrays that evaporated 2.17 kg m^{-2} h^{-1}
95 , and Zhang et al. [31] created a tower-shaped evaporator using a magnetically driven spray-
96 coating method, evaporating at 1.59 kg m^{-2} h^{-1}. All these studies claim that the radiation
97 reflected from a surface can be reabsorbed by another part of the material. The evaporation
98 rates were close to values of 2 kg m^{-2} h^{-1}, and all materials had an evaporative area greater
99 than the area projected on the ground.

100 In this paper, a novel approach of combining a carbon nanomaterial and 3D printing is
101 used to study different types of geometries using experimental measurements and numerical
102 modelling. The originality of this work consists in: (i) using a 3D-printed structure mixed with

AC powder as an evaporation material under a convective flow; and (ii) integrating fluid mechanics around the evaporator and surface-to-surface radiation in a numerical model in order to understand the different physical phenomena that improve the evaporation flow. A 2D flat surface and four different 3D structures are studied here to investigate the phenomena that occur during evaporation. Experimental evaporation results as well as simulation results are shown, and then the effect of surface-to-surface radiation in concavities is studied. A study of the evaporation of the illuminated top surface is conducted, followed by a parametric study on the height of the paraboloid. Then, a study on the heat exchange coefficients on each side of each material is carried out based on the simulation results. Finally, the effect of perforation of a 3D paraboloid structure is investigated using simulation results of evaporation under natural convection.

2 Materials and Methods

2.1 Evaporation materials

Five geometries were studied: a 2D flat surface and four 3D structures, namely an inverted cone, a sphere, and a paraboloid of revolution, without or with holes. Each material was first drawn on COMSOL and designed using the CAD software NAUTA (DWS, Italy), and then printed using a DWS J28 high-resolution 3D printer (desktop SLA), Invicta DL380 resin (DWS, Italy) and a class 1 laser (λ = 405 nm, 32 mW) with a laser spot size of 17 µm. The resulting geometries had a grid pattern, with a spacing such that the empty spaces could be manually filled with AC and had a uniform surface on the sides and top of the geometries. The resulting 3D-printed structure only serves as a skeleton, which is filled with AC, and does not diffuse water itself. The PULSORB WP270 AC was obtained from Chemviron, a Kuraray Company, and used in all experiments. The process of fabricating the structures is shown in **Fig. 1**, along with the subsequent 3D geometries used in the model and in the experiments.

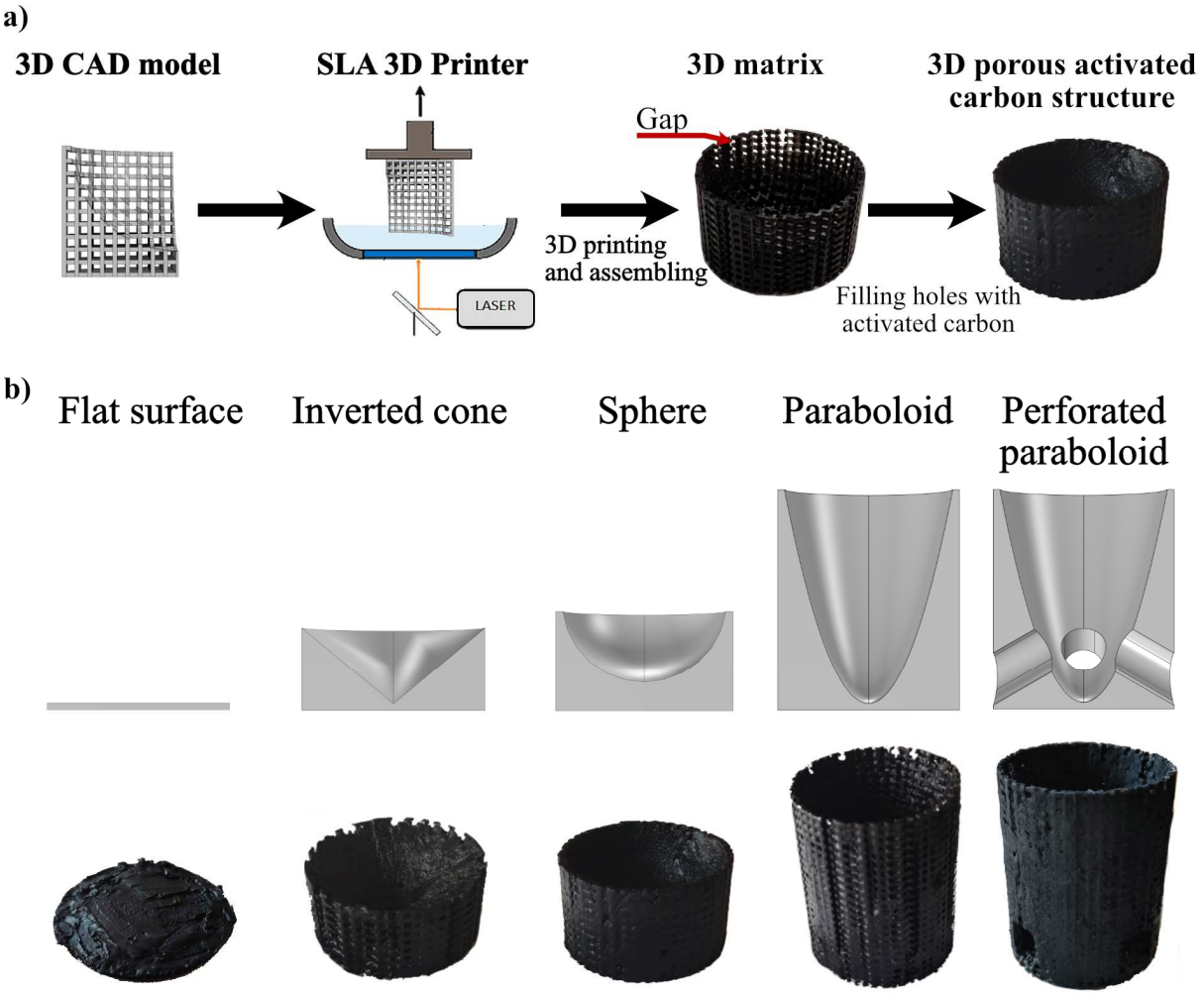

Fig. 1. a) 3D printing process to obtain a 3D porous structure, followed by filling is empty spaces with activated carbon; b) geometries used in the model and photos of the 3D structures filled with activated carbon.

2.2 Experimental protocol and measurement methods

In a typical experiment, a beaker (internal diameter 58 mm) is illuminated by a solar light simulator (SOLAR LIGHT LS-1000). A layer of insulating foam surrounds the beaker, and the foam is covered with an aluminium foil to limit heat transfer by convection and radiation with the outside. The beaker is filled with tap water and a polystyrene foam floats on the surface. Around this foam, cotton is used to transport the water to the surface, where the material with AC is located. An aperture is used to limit the solar light to the diameter of the beaker and avoid residual heating around it. The experimental setup is shown in **Fig. 2**. A

Sartorius ENTRIS balance, accurate to the milligram, is used to measure the mass of the entire system, which allows the calculation of the amount of evaporated water by difference.

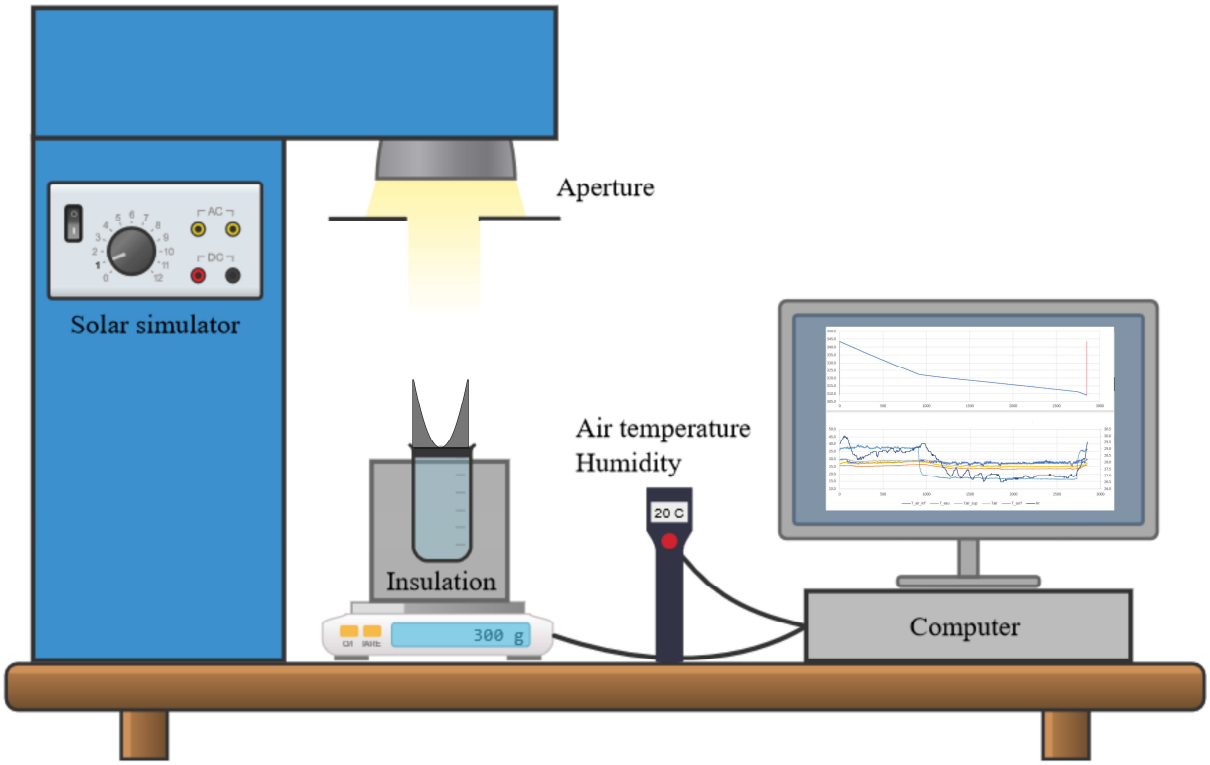

Fig. 2. Experimental setup used to measure the evaporation rate of water with activated carbon at the surface.

2.3 Standardisation of ambient condition at 20°C

Due to the changing ambient conditions, the results often vary over the course of a day as the air temperature increases. In order to reason at the same level of performance, a linear regression method is chosen in this study. A material is tested throughout the day and the mass change results are calculated every half hour. A linear regression of the evaporation rate against air temperature is then performed. With the baseline thus obtained, the evaporation rate at 20°C is calculated and, in this way, all materials can be compared at the same performance level. Although this method does not take into account the humidity of air, which can vary from day to day, and the type of convection that occurs around the system, previous research has shown that temperature plays a more important role than humidity [6].

3 Physical model

The solar simulator used in this study is cooled by several fans since its output power is close to 1 kW. To study the flow around the structure, a 3D model was written using COMSOL Multiphysics 6.0. The paraboloid evaporation material model is shown in **Fig. 3**. In the experiment and in the model, the top surface is illuminated by solar radiation, is cooled by convection with air, and evaporates water as shown in **Fig. 3a**. At the bottom, there is only conduction, with a fixed heat transfer coefficient.

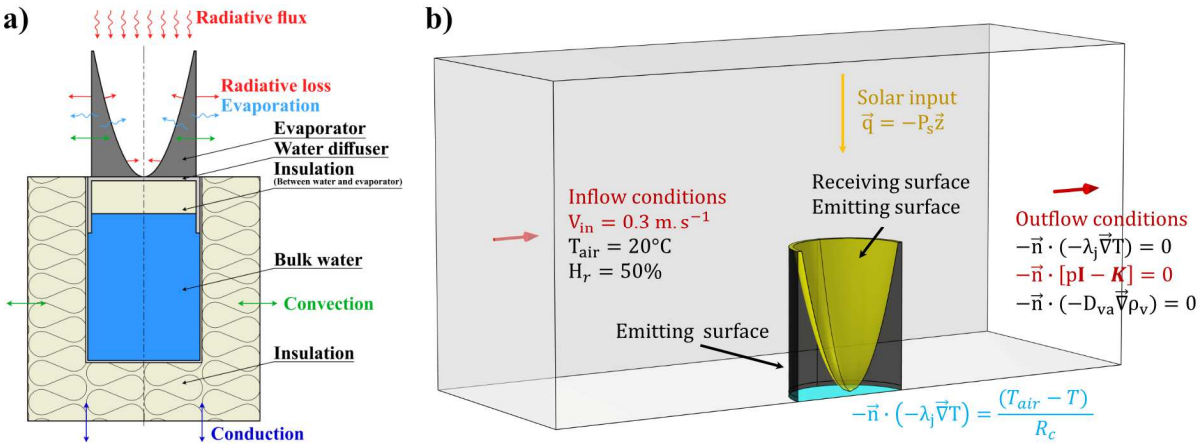

Fig. 3. a) Schematic of the experimental evaporation system and the physics involved; and b) schematic of the boundary conditions set in the simulation (only the computed section is shown here).

3.1 General equations

In order to simulate the heat and mass transfers existing during the evaporation process, the energy and mass conservation equations were used to obtain the temperature, T (Eq. 1), the fluid flow velocity, $\vec{u}$ (Eq. 2 and Eq. 3), and the partial density of the vapour in air, ρ_v (Eq. 5).

The energy conservation equation describes conductive heat transfer and temperature changes over time. The heat transfer equation is therefore written as:

$$\rho_j c_{p,j}\vec{u}\cdot\vec{\nabla}T + \vec{\nabla}\cdot\left(-\lambda_j\vec{\nabla}T\right) = 0 \qquad \text{Eq. 1}$$

where ρ_j (kg m^{-3}) is the density, $c_{p.j}$ (J kg^{-1} K^{-1}) is the heat capacity, $\vec{u}$ (m s^{-1}) is the air flow velocity and λ_j (W m^{-1} K^{-1}) is the thermal conductivity of component *j* (evaporation material, *m* or air, *a*).

The fluid flow velocity is described by the stationary Navier-Stokes (Eq. 2) and mass conservation (Eq. 3) equations.

$$\rho_a(\vec{u}\cdot\vec{\nabla})\vec{u} = \vec{\nabla}\cdot\left[-p\boldsymbol{I} + \mu(\nabla\vec{u} + (\nabla\vec{u})^T) - \frac{2}{3}\mu(\vec{\nabla}\cdot\vec{u})\boldsymbol{I}\right] - \rho_a\vec{g} \quad \text{Eq. 2}$$

$$\vec{\nabla}\cdot(\rho_a\vec{u}) = 0 \quad \text{Eq. 3}$$

where p (Pa) is the pressure, μ (Pa s) the dynamic viscosity of air and $\vec{g}$ (m s^{-2}) the gravitational acceleration. ρ_a (kg m^{-3}) is the density of air and is calculated as follows:

$$\rho_a = \frac{pM_a}{RT} \quad \text{Eq. 4}$$

where R (J mol^{-1} K^{-1}) is the universal gas constant and M_a (kg mol^{-1}) is the molar mass of air.

The transfer of water vapour is described by the phenomenon of water diffusion in air (Eq. 5):

$$\vec{\nabla}\cdot\left(\rho_v\vec{u} - D_{va}\vec{\nabla}\rho_v\right) = 0 \quad \text{Eq. 5}$$

where D_{va} (m² s^{-1}) is the diffusion coefficient of vapour in air.

3.2 Boundary conditions

In this section, the boundary conditions used are given. It should be noted that thermal continuity conditions are used in the heat equation (Eq. 1) for all internal boundaries. The boundary conditions are also shown in **Fig. 3b**.

3.2.1 Air-material interface

The heat exchange at the surface (Eq. 6) takes into account convection, incoming light radiation, as well as losses through emission and water evaporation (**Fig. 3**). Water

evaporation involves the surface evaporation rate, $\dot{m}_{surf}$ (kg m^{-2} h^{-1}), multiplied by the energy consumed to raise the water temperature and the enthalpy of vaporisation of water, h_v (J kg^{-1}).

$$-\vec{n}\cdot\left(-\lambda_m\vec{\nabla}T\right) = -\vec{n}\cdot\left(\rho_a c_{p,a} T\vec{u} - \lambda_a\vec{\nabla}T\right) - \dot{m}_{surf}\left(h_v + c_{p,w}(T - T_{ref})\right) + P_r \quad \text{Eq. 6}$$

where λ_m (W m^{-1} K^{-1}) is the thermal conductivity of the evaporation material, ρ_a (kg m^{-3}) is the thermal density of air, $c_{p,a}$ (J kg^{-1} K^{-1}) is the heat capacity of air, λ_a (W m^{-1} K^{-1}) is the thermal conductivity of air, T_{ref} (273.15 K) is the reference temperature, P_r (W m^{-2}) the power density source term from the surface-to-surface radiation equation and $-\vec{n}$ the unit vector normal to the boundary.

The surface-to-surface radiation uses a set of equations from the COMSOL surface-to-surface radiation toolbox. The power source term from the sun, P_s (W.m^{-2}), is set so that the solar power is applied on the axis perpendicular to the material. This toolbox allows each surface to exchange heat with each other where possible and to interact with the ambient air and the solar energy source. Therefore, P_r is used to represent the power density source term from the surface-to-surface toolbox.

At the upper surface, the water loss in the diffusivity equation is equal to the evaporation rate:

$$-\vec{n}\left(\rho_v\vec{u} - D_{va}\vec{\nabla}\rho_v\right) = \dot{m}_{surf} \quad \text{Eq. 7}$$

The surface of the material is considered to be saturated with liquid water. Since the evaporation of water comes from the difference in mass concentration between the surface and the air, then $\dot{m}_{surf}$ is calculated as follows [32]:

$$\dot{m}_{surf} = -K\left(\rho_{v,sat} - \rho_v\right) \quad \text{Eq. 8}$$

where K (m s^{-1}) is the convective mass exchange coefficient. In addition, the partial density of the vapour at the air-material boundary, considered to be saturated, $\rho_{v,sat}$ (kg.m^{-3}), is calculated as follows:

$$\rho_{v,sat} = \frac{P_{v,sat} M_v}{RT} \quad \text{Eq. 9}$$

where M_v (kg mol^{-1}) is the molar mass of water. The water vapour pressure at a given temperature T, $P_{v,sat}$ (Pa), is calculated as follows:

$$P_{v,sat} = P_0 \, exp\left(\frac{h_v}{R} M_v \left(\frac{1}{T_0} - \frac{1}{T}\right)\right) \quad \text{Eq. 10}$$

where P_0 (101 325 Pa) is the reference pressure and T_0 (373.15 K) is the boiling temperature of water.

3.2.2 Interface between the bulk water and the bottom of the material

At the interface between the bulk water and the bottom of the material, conductive heat transfer occurs. For simplicity, the conductive heat flux is represented as follows with an overall thermal resistance and a fixed air temperature:

$$-\vec{n}\left(-\lambda_m \vec{\nabla} T\right) = \frac{(T_a - T)}{R_c} \quad \text{Eq. 11}$$

where R_c (m^2 K^1 W^{-1}) is the thermal resistance between the material and the bulk water, and T_a (K) is the air temperature source term.

3.2.3 Air inflow, outflow and other boundaries

During the experiment, the air flow velocity, M_v, was measured and found to be 0.3 m s^{-1}. The latter value and the temperature of the air entering the domain, set at 20°C, were used to calculate the partial density of water using the following equation:

$$\rho_{v,in} = \frac{P_{v,sat,20} M_v}{RT} H_r \quad \text{Eq. 12}$$

where $P_{v,sat,20}$ (Pa) is the water vapour pressure at 20°C calculated using Eq. 10, the temperature, *T,* and relative humidity, H_r, being 293.15 K and 50%, respectively.

Other boundaries, shown in grey in **Fig. 3b**, also have these values of *T* and H_r, and are also considered as walls for flow physics. A symmetry plane passing through the middle of the structure, in the direction of flow, is used to reduce the computational cost, allowing only half of the geometry to be calculated. **Fig. 3b** shows the calculated section.

3.3 Simulation parameters

Table 1 lists the input parameters used in the simulation, and their symbols, definitions, units and values considered are also given.

Table 1. Input parameters used in the simulation.

Symbols	Definitions	Units	Values
λ_w, λ_m, λ_a	Thermal conductivities of water, evaporation material and air	W m^{-1} K^{-1}	0.6, 0.59, 0.0262
$c_{p,w}$ $c_{p,air}$	Heat capacities of water and air	J K^{-1} kg^{-1}	4180, 1004
μ	Dynamic viscosity of air	Pa s	18.5×10^{-6}
D_{va}	Diffusion coefficient of water inside the material	m^2 s^{-1}	2.82×10^{-5}
h_v	Vaporisation enthalpy of water	kJ kg^{-1}	2453
ρ_w	Density of water	kg m^{-3}	1000
R	Universal gas constant	J mol^{-1} K^{-1}	8.314
M_v, M_a	Molar mass of water and air	kg mol^{-1}	0.01801, 0.02897
P_0	Standard pressure	Pa	101325
T_0, T_{ref}, T_a	Boiling point temperature of water, reference temperature, intake air temperature	K	373.151, 273.15, 293.15
R_c	Thermal resistance between material and bulk water	m^2 K^1 W^{-1}	0.2

3.3.1 Numerical model

The model used in this study consists of two components. One represents the evaporation material, with its geometry, and the other represents the air surrounding the material. A coarse

mesh is used for the air geometry and a finer mesh is set up on the boundary between the air and the material. For instance, 38301 elements were used to model the paraboloid case and, using two Xeon Silver 4214R CPUs (24 cores) combined with 256 GB of RAM, the model was computed in 4 minutes and 30 seconds.

4 Results and discussion

4.1 Comparison between simulation and experiments

Fig. 4a shows the evaporation performance for all printed geometries, as well as for a flat surface of AC and bulk water. Each result is linearly dependent on temperature, so a linear regression can be performed to determine an evaporation value at 20°C. All geometries showed a linear trend with a particularity for the perforated paraboloid, which was more dependent on air temperature than the others. At 20°C, the experimental evaporation rates were 0.53, 1.34, 1.41, 1.91 and 1.91 kg m^{-2} h^{-1}, for the flat, conical, spherical, paraboloid and perforated paraboloid geometries, respectively. The latter results are shown in **Fig. 4b**, together with the simulated results for each geometry, as a function of the total evaporation area, which includes both the illuminated area and the side of the geometries. It is evident that evaporation increases linearly with the total evaporation area. The simulated evaporation rates were 0.88, 1.63, 1.61, 1.94 and 1.97 kg m^{-2} h^{-1} for the flat, triangular, spherical, paraboloid and perforated paraboloid geometries, respectively.

3D materials come in all shapes and sizes, making them difficult to compare as the projected area is usually different and the air conditions, i.e., temperature, relative humidity (RH) and air convection, are affected by the exchanges that occur on the cold surfaces. Knowing this and taking a temperature of 20 °C, RH of 50% and low convective flow as a reference case, the perforated paraboloid evaporates at 1.91 kg m^{-2} h^{-1}. A similar 3D cup-shaped material was fabricated by Shi et al. and had at least 50% more evaporative area than

the perforated paraboloid presented here, and evaporated at 2.04 kg m^{-2} h^{-1} under one sun illumination. Table S1 shows the performance of several 3D reference materials. Materials with a high total surface area relative to the projected area have been purposely left out of this table, as they will be used in arrays under real outdoor conditions that will artificially increase their evaporation rate. The average of these results is 2.25 kg m^{-2} h^{-1} and the perforated paraboloid presented here is positioned not far from what is currently achieved, 1.91 kg m^{-2} h^{-1}. In addition, our design approach is different from what has been done previously. 3D printing allows a wide variety of geometries to be precisely fabricated, for example to improve the evaporative area or to improve the exchange under high airflow. However, the paraboloid presented here would be difficult to make by hand and the limitations of this approach are the cost of the resin, which contrasts with materials made from waste, such as egg cartons and used ink for instance [21]. The 3D-printed skeleton is nevertheless robust, can be cleaned of any dirt and the AC can be replaced if necessary.

It was found that the fan cooling the xenon lamp, which is positioned at the rear of the evaporation system as shown in **Fig. 4c** and **Fig. 4d**, creates an air flow around the material with an air velocity of 0.4 m s^{-1}. A smoke test was therefore carried out and revealed that the convection was forced due to the cooling of the xenon lamp. **Fig. 4c and Fig. 4d** show the smoke from the front and side of the system. From the side, the flow passes over the geometry and some of it can be seen flowing inside the paraboloid. From the front, the flow goes around the side of the geometry. The simulated flow, calculated using Eqs. 2 and 3, is shown in **Fig. 4e** and **Fig. 4f** with similar behaviour to the smoke test. A vortex is visible behind the geometry, which was not visible in the smoke test.

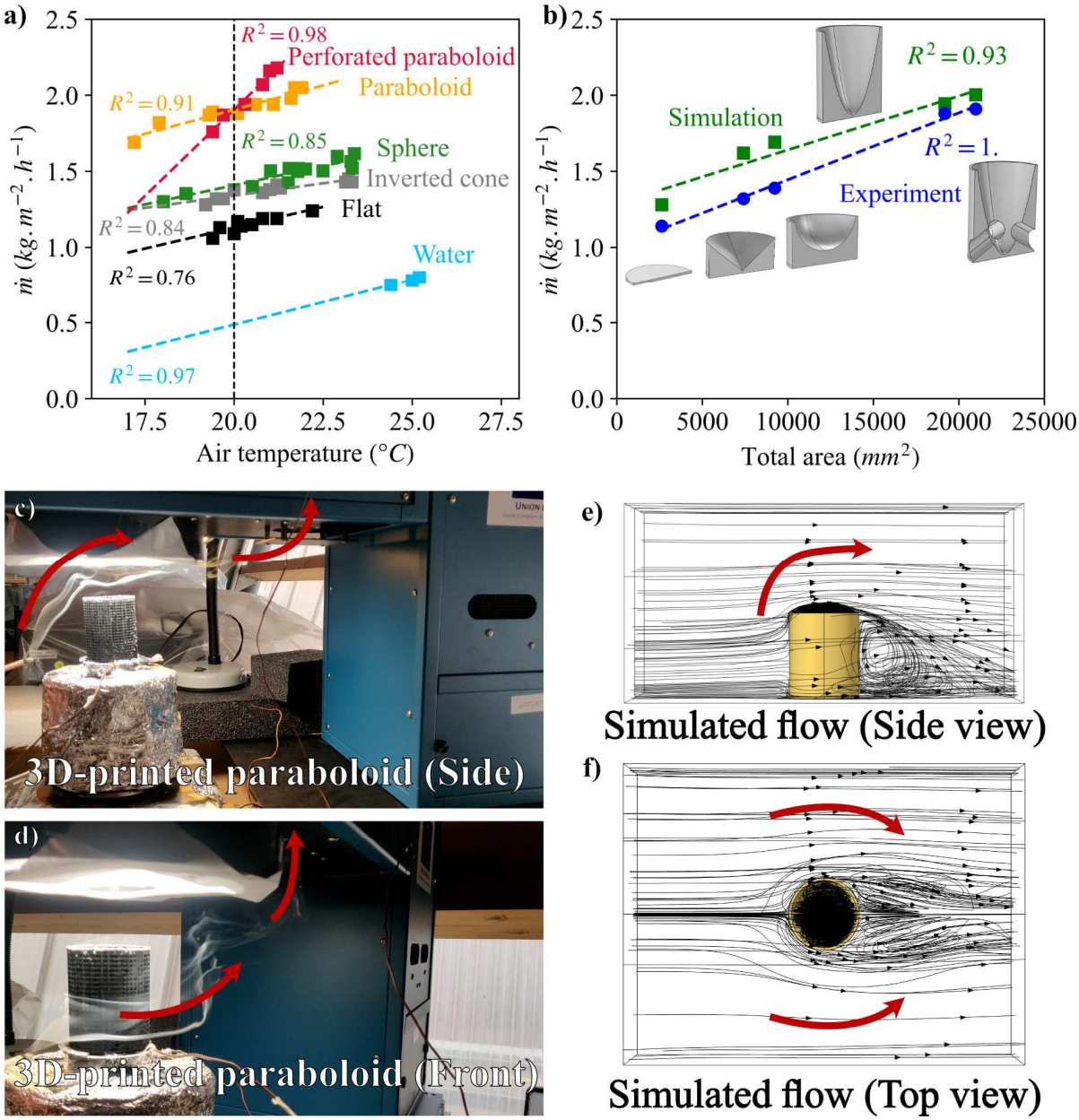

Fig. 4. a) Linear regressions of experimental results of evaporation rate for each geometry; b) simulated and experimental evaporation rate as a function of total evaporation area; smoke test for the paraboloid geometry seen from: c) side, and d) front; simulated air flow velocity streamlines seen from the: e) side, and f) top.

Fig. 5a to **Fig. 5e** show the relative humidity distribution for the different geometries and **Fig. 5f** to **Fig. 5j** show the temperature distribution. With these simulations, it can also be observed that the air coming into contact with the geometry becomes loaded with moisture and increases its temperature. This shows that the mass and heat transfers are transverse and therefore driven by the airflow created by the fan used to cool the solar simulator. This

observation, coupled with the experimental ones (in **Fig. 4)**, validates the hypothesis of using a 3D model to study the heat and mass transfers. When natural convection is predominant and vertical transfer is observed, a 2D axisymmetric simulation is sufficient. In addition, a vortex is visible behind each geometry, which enhances heat and mass transfer and thus evaporation.

It can be observed that the triangular, spherical and paraboloid geometries have the same type of flow inside, showing a vortex. The perforated paraboloid geometry, on the other hand, has a bottom-up flow, with the rear hole also acting as an inlet. The air intake at the bottom allows this geometry to accelerate the transfers inside, which can be seen in **Fig. 4a** where the linear regression of the paraboloid shows a more sensitive behaviour to temperature change. Between the geometries, similar behaviours are noticeable. The temperature is always higher at the centre of the geometry, i.e., at the tip of the cone, at the base of the sphere or at the base of the paraboloid. Similarly, the larger the geometry, the lower the internal temperature, which is due to the distribution of radiation over a larger area as well as evaporation losses. Generally, a higher surface temperature is desirable for evaporation [6], but in this case it can also be a means of exploiting the energy from the air [33]. Indeed, if the surface is cooler than the air, the exchange between the two is beneficial, which is the case at several points for both paraboloids.

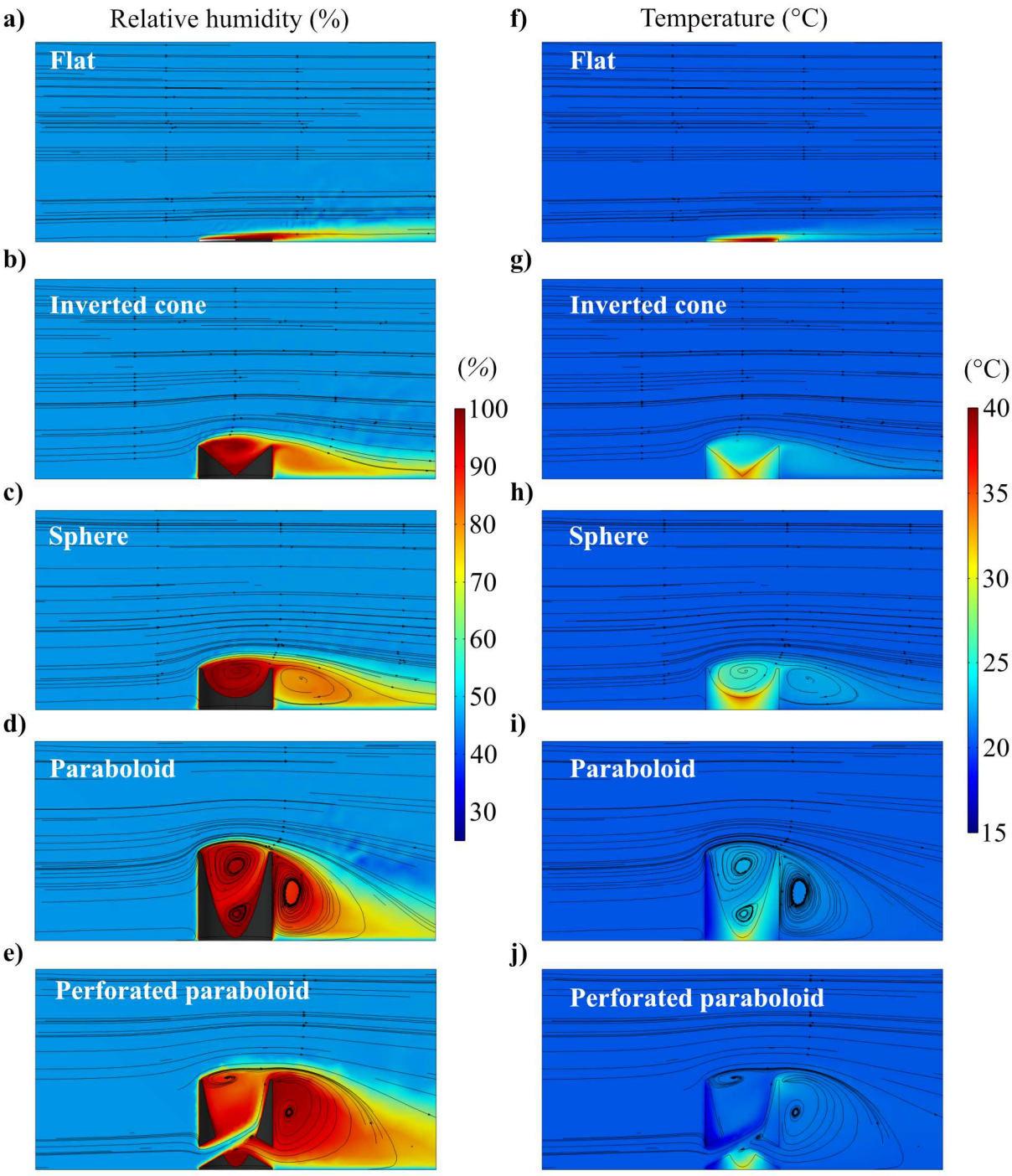

322

323 **Fig. 5.** a) to e) Relative humidity and air flow velocity streamlines; and f) to j) temperature
324 seen on a plane placed in the middle of the domain for each geometry.

325

4.2 Surface-to-surface radiation study

A common assumption in the literature is that having a concave spherical evaporation surface increases the evaporation rate [29,34]. The theory is that by reflecting solar radiation from one side of the surface to the other, using a sphere for instance, a greater efficiency can be achieved. The geometries used in this study were made to test this hypothesis. Each can collect sunlight differently, with an inverted conical, spherical and paraboloid surface. **Fig. 6a** shows the simulated results with surface-to-surface radiation, which means that each surface can interact with the other, emitting and receiving. Another simulation result shows only the radiation losses with air. The difference between the two is the ability to receive from the other surface. It can be seen that surface-to-surface radiation has a minor role in evaporation performance, with only a 1% increase between the evaporation rates with and without surface-to-surface radiation. Zhao et al. fabricated a conical hydrogel that evaporated 17% better than its 2D counterpart and hypothesized that light scattering was a factor in the improvement [28], while the conical geometry presented here improves by 26% the performance of the 2D geometry. These slight performance improvements can be attributed to the increased area rather than light reflection. Thus, surface-to-surface radiation cannot drastically increase performance, and priority should be given to increasing the evaporation area.

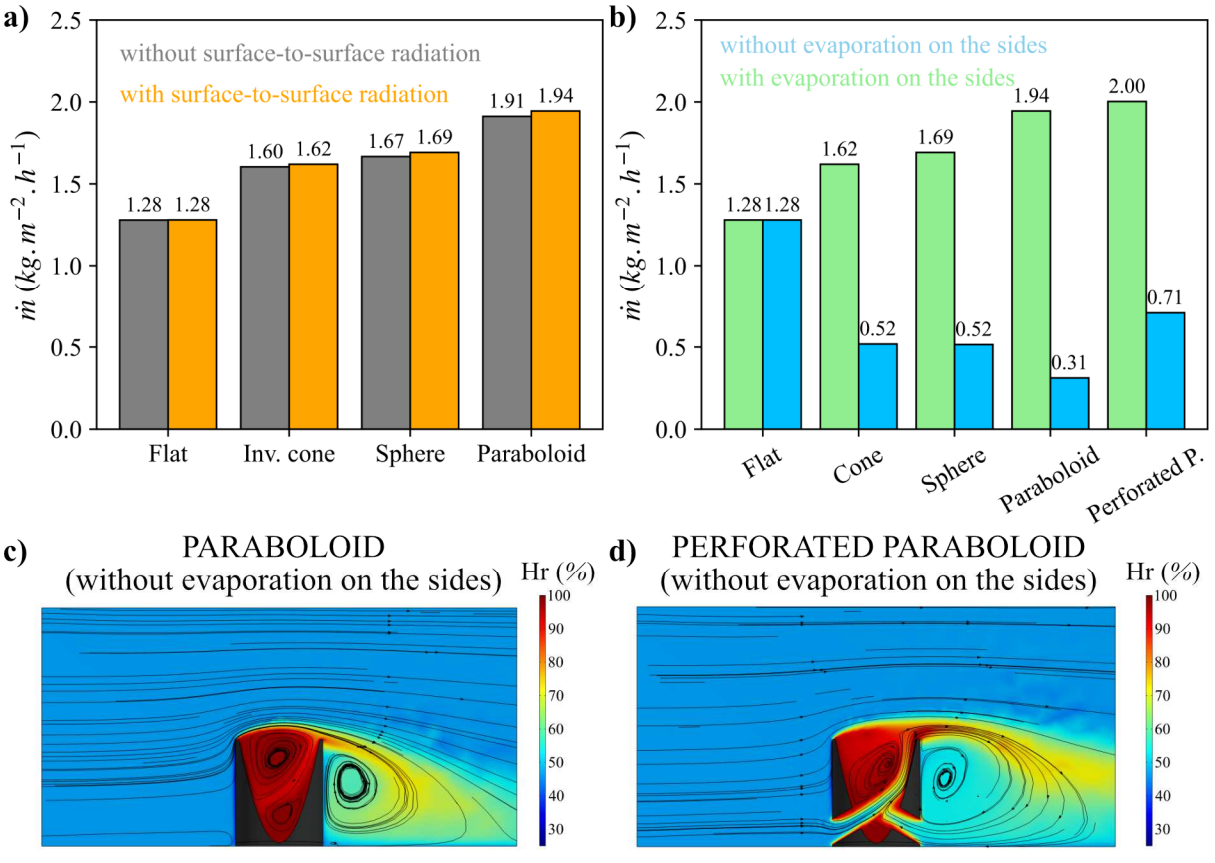

Fig. 6. a) Simulated evaporation rates with and without surface-to-surface radiation; and b) simulated total evaporation rate and evaporation rate on the top surface only; humidity profile for the case without evaporation on the sides for: c) the paraboloid, and d) the perforated paraboloid; humidity profile for the case with evaporation on the sides for: e) the paraboloid, and f) the perforated paraboloid.

4.3 Results without evaporation on the sides

Fig. 6b shows the simulated evaporation performance of the standard case at 20°C, presented earlier, compared to a case set so that no evaporation is possible on the sides of the geometries. The simulated evaporation rates for the inverted cone, sphere and paraboloid are lower than the results for the flat material, the sphere being the lowest of the three with an evaporation rate of 0.41 kg m^{-2} h^{-1}, followed by the paraboloid with 0.43 kg m^{-2} h^{-1} and the inverted cone with 0.54 kg m^{-2} h^{-1}. In contrast to the others, the perforated paraboloid outperforms the flat surface without evaporation on the sides, with an evaporation rate of 0.78 kg m^{-2} h^{-1}.

These results show that the concave evaporators do not perform well without the possibility of evaporating on their sides. Furthermore, the simulated evaporation rate does not change in the same way with the variation in evaporation area as when all surfaces evaporate. The paraboloid, which has more than twice the area of the inverted cone, does not perform better. This is because a larger area is enclosed in the paraboloid (**Fig. 6c**), so the airflow cannot penetrate it, whereas it can enter the geometry of the inverted cone, which is more open, and thus allows vapour-saturated air to escape. As can be seen in **Fig. 6d**, this is not the case for the perforated paraboloid: as air can enter from below, more vapour-saturated air can be exhausted and, with the renewed air, evaporation increases. This behaviour is only partially possible as long as evaporation from the sides is possible, since the air coming from the rear of the geometry is already saturated with water vapour (**Fig. 5e**).

4.4 Parametric study on the paraboloid geometry

To study the effect of the total evaporation area on performance, a parametric study was conducted with the paraboloid geometry. The parameter changed was the coefficient of the parametric curve of the paraboloid, which defines the curvature as well as the height of the geometry, thus increasing or decreasing the evaporation area. As can be clearly seen in **Fig. 7a**, the total evaporation from the surface determines the evaporation rate, meaning that a higher area implies a higher evaporation rate, ranging from 1.5 kg m^{-2} h^{-1} for an area of 3962 mm^2 to 2.0 kg m^{-2} h^{-1} for the highest paraboloid with an area of 19181 mm^2 (i.e., the paraboloid presented earlier).

It should also be noted that while evaporation on the sides increases with the size of the geometry, evaporation on the illuminated surface reduces. In fact, as can be seen in **Fig. 7c-f** showing the humidity for the four different geometries, the air on the upper side of the paraboloid is saturated with vapour, which limits the potential evaporation (Eq. 8). In the end,

384 the total evaporation only increases due to the total evaporation area and the shape of the
385 geometry has little impact on the performance. As shown in **Fig. 7b**, the evaporation rate
386 calculated using the total surface area, i.e., including the sides and interior, instead of the
387 projected area, i.e., the disk illuminated by solar radiation, decreases as the total area
388 increases. The usually calculated evaporation rates are only higher due to the increase of the
389 ratio between the projected area and the total area. This behaviour should be true until the
390 limit of water transport within the material is reached, and water can no longer progress
391 further into the geometry. For this reason, recent studies have used materials with high ratio of
392 total area to projected area [35], allowing very high evaporation rates up to 7.6 kg m^{-2} h^{-1}.

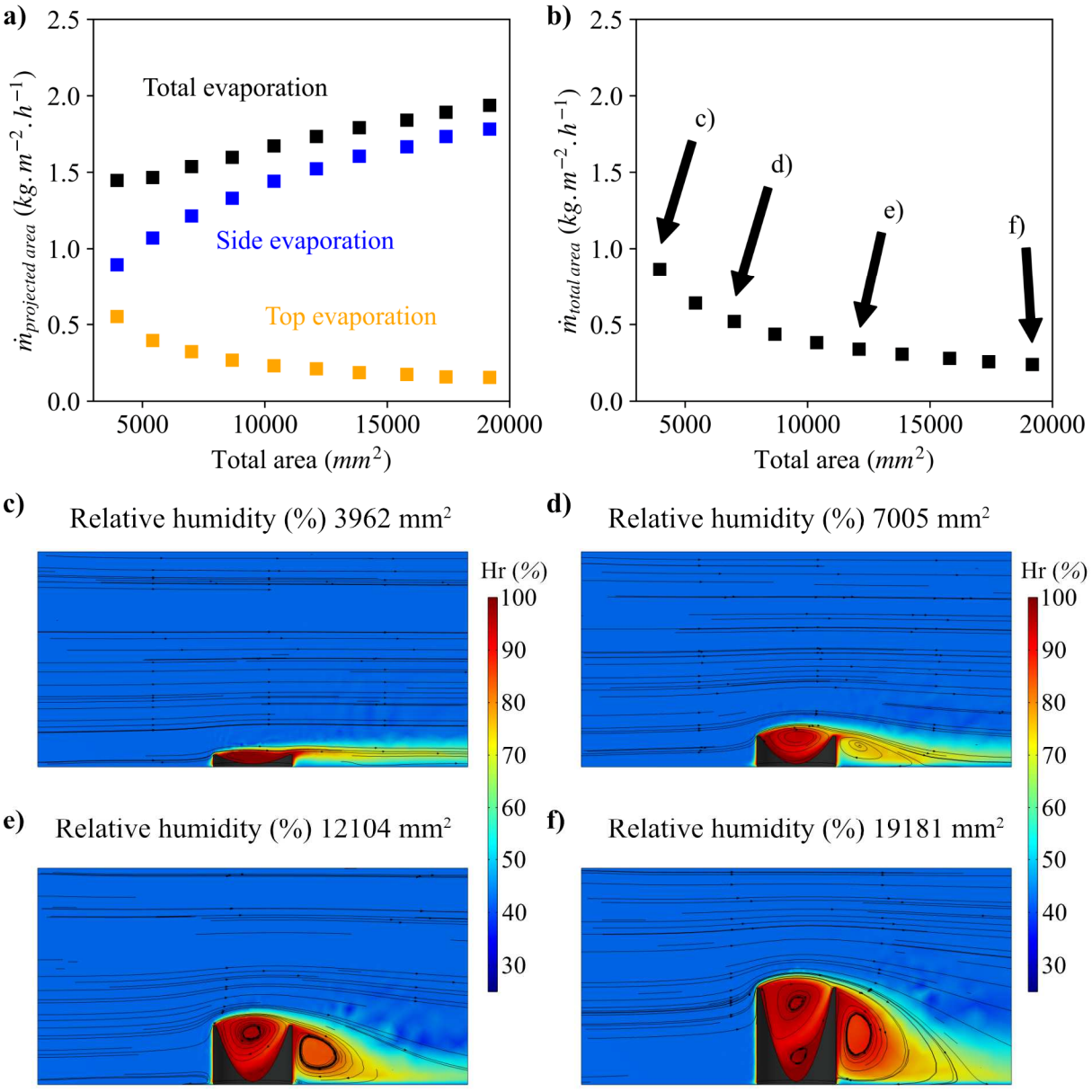

Fig. 7. a) Evaporation rate over the total, side and illuminated area calculated using the projected area as a function of the total evaporation area; b) Evaporation rate calculated using the total evaporation area; Humidity plots and air flow velocity streamlines for the cases with a total area of: c) 3962 mm^2, d) 7005 mm^2, e) 12104 mm^2, and f) 19181 mm^2.

4.5 Exchange coefficients on different sides

Despite the absence of saturated air evacuation, the heat exchange varies with each geometry. In the case where the surrounding air is not simulated by fluid dynamics, the heat exchange is considered by introducing the convective heat transfer coefficient, which is

difficult to estimate when using complex geometries [6]. Therefore, this section proposes to study the impact of geometry on the convective heat transfer coefficient. **Fig. 8** shows the different convective heat transfer coefficients along a line in the middle and on the sides of the geometry for the cases presented in section **4.1**. The coefficient was calculated from the heat flow conservation equation (Eq. 6) as follows:

$$-\vec{n}\left(-\lambda_m \vec{\nabla} T\right) = h_c(T_a - T) - \dot{m}_{surf}\left(h_v + \mathrm{c_{p,w}}(\mathrm{T} - \mathrm{T_{ref}})\right) + P_r \qquad \text{Eq. 13}$$

where λ_m (W m^{-1} K^{-1}) is again the thermal conductivity of the material, h_c (W m^{-2} h^{-1}) is the heat transfer coefficient, T_a (°C) is the air temperature, set here at 20°C as shown in **Table 1**, and P_r (W m^{-2}) is the power density source term from the surface-to-surface radiation equation.

The different structures are shown in the middle of **Fig. 8a**, and the corresponding heat transfer coefficient are plotted on its sides: front, top and rear. Since the front is shown on the left, where the air flow originates, the $\boldsymbol{x}$-axis is positive on the left and negative on the right. In addition, the top plot shows h_c as a function of the $\boldsymbol{x}$-axis and the front and rear graphs show h_c as a function of the $\boldsymbol{y}$-axis. In this study, it is the general behaviour that is sought, rather than the local values or boundary effect, in order to see how the exchanges occur according to the geometry. Firstly, at the front and rear surfaces, the left and right graphs respectively, the heat transfers are more predictable. For the tall cylinders, which are both paraboloids, the heat transfer at the front is constant with values around 16 W m^{-2} K^{-1}, while the smaller cylinders, which are the inverted cone and the sphere, show a maximum value near the top (25 W m^{-2} K^{-1}), which decreases to a minimum value at the base (10 W m^{-2} K^{-1}). These values reflect the fact that the airflow arrives perpendicular to the cylinder without disturbance, which allows a high heat transfer. This is not the case at the rear of the geometries, as all of them have a vortex that starts from the top and returns to their rear side

(**Fig. 5**). This results in a curve with a maximum value of heat transfer coefficient where the flow arrives at the rear of the geometries, of 10 W m^{-2} K^{-1} for all geometries except the perforated paraboloid, which has a higher vortex and a maximum coefficient of 5 W m^{-2} K^{-1}. However, these values are lower than those of the front face since the flow velocity is reduced by the presence of the structures as can be seen in **Fig. 8b** and **8c**.

The flat surface, shown only on the top surface, has a more uniform coefficient of about 10 W m^{-2} K^{-1}. Although the value increases at the front boundary, since the amount of surface area per heat transfer is small, the flat surface transfers homogeneously because the flow is not disturbed by its presence. Compared to the behaviour of the flat surface, the other geometries have an h_c profile that depends on the convection that occurs at the top. They all show a vortex effect, visible in **Fig. 5b-d**, which starts from the rear side of the top surface, where the flow touches the structure, and then moves inwards through the centre of the concave geometry and then to the front side of the top geometry. This vortex is directly visible on the heat transfer coefficient, since air flowing over a surface results in higher heat transfer. As a result, the inverted cone, sphere and paraboloid each show a high value at the rear (right of the graph) and decrease to a low value below 8 W m^{-2} K^{-1}, then increase again at the front (left of the graph). The paraboloid has a steeper curve at the front, with an increasing value that is above 15 W m^{-2} K^{-1}, a figure that the sphere and the inverted cone do not exceed.

The perforated paraboloid, however, shows a different behaviour that is caused by the flow through the holes. In fact, as can be seen in **Fig. 8c,** the flow inside the holes at the front of the perforated paraboloid goes fast, which directly translates into a high h_c value of 40 W m^{-2} K^{-1}, visible in blue on the right of the upper graph, where the hole starts. The heat transfer gets high and then decreases. However, due to the air flow, this behaviour is not symmetrical, so that the front side of the top surface does not show as high a transfer. Holes are therefore thermally beneficial, as they increase mass transfer and thus heat transfer, but as the air is so

quickly saturated, this effect hardly translates into increased evaporation. Ultimately, it was found that cylindrical and concave structures do not exploit the potential of forced convection to improve mass and heat exchanges. Further design improvements are needed to enable even greater evaporation performance.

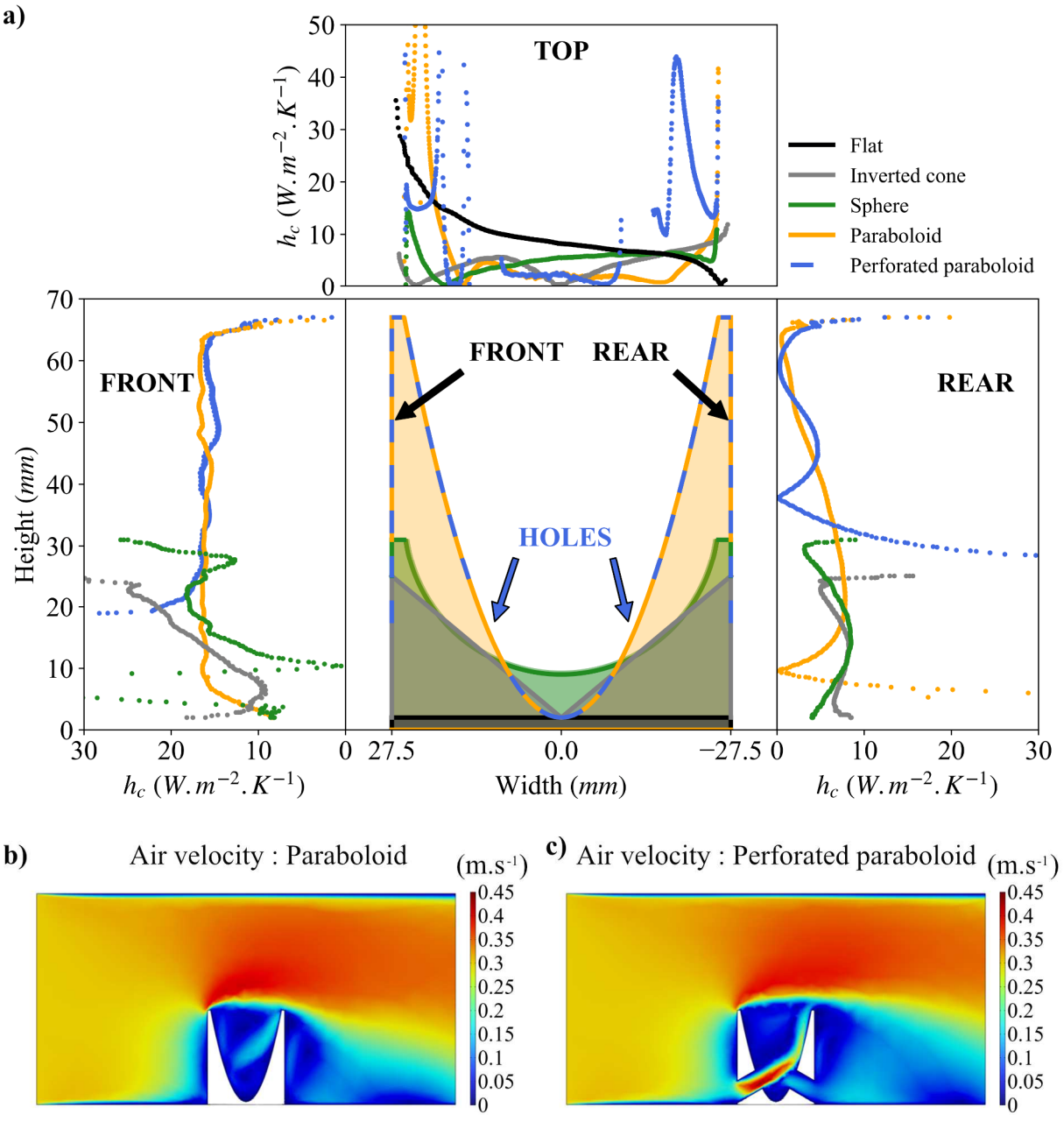

Fig. 8. a) Heat transfer coefficient on the front side, rear side and top surface; air velocity profile for the: b) paraboloid, and c) perforated paraboloid.

4.6 Simulated evaporation under natural convection

The experimental results were found to be under forced convection, which increases the evaporation performance and establishes a horizontal flow compared to a natural convection flow. To investigate this effect, a natural convection was simulated, where the inflow and outflow were supressed.

Fig. 9a shows the results for forced and natural convection for all geometries. **Fig. 9b and c** show the relative humidity distribution and flow. In the case of natural convection, the flow is directed upwards, as is the humidity. Under natural convection, the evaporation increases with the total area of evaporation but to a lesser extent than under forced convection. Thus, when switching from forced to natural convection, the evaporation on the flat surface decreases only from 0.90 to 0.82 kg m^{-2} h^{-1}, while that of the paraboloid decreases from 2.0 to 1.6 kg m^{-2} h^{-1}. Despite the added holes, the perforated paraboloid has only a slightly higher evaporation rate than the paraboloid, from 2.01 kg m^{-2} h^{-1} under forced convection to 1.68 kg m^{-2} h^{-1} under natural convection. While the holes allow air to pass inside the structure, as can be seen in **Fig. 9c**, the air flow is not directed towards the surface and instead passes through the middle of the paraboloid. Kim et al. [36] observed the same phenomenon with a chimney-type structure that allows air to flow through the centre of the evaporators, but since the air flow is induced in the centre and not directed towards the evaporating surface, the improvement is limited. To investigate the effect of the geometry on flow in more detail, the heat transfer coefficients have been calculated and are shown in **Fig. 9d**. The front and rear of the cylinder around the paraboloids show symmetrical behaviour for both paraboloids, since the flow is not forced in one direction. The top surface, however, has a slightly higher heat transfer coefficient on the sides of the top surface. Although the holes allow more air to circulate, the coefficient remains low and evaporation is not significantly improved.

Ultimately, under natural or forced convection, the geometries showed that control of airflow is the key to improving evaporative performance. Allowing air to flow, opening the geometry and controlling the direction of flow to improve heat transfer over the evaporation surface should be a priority in future studies.

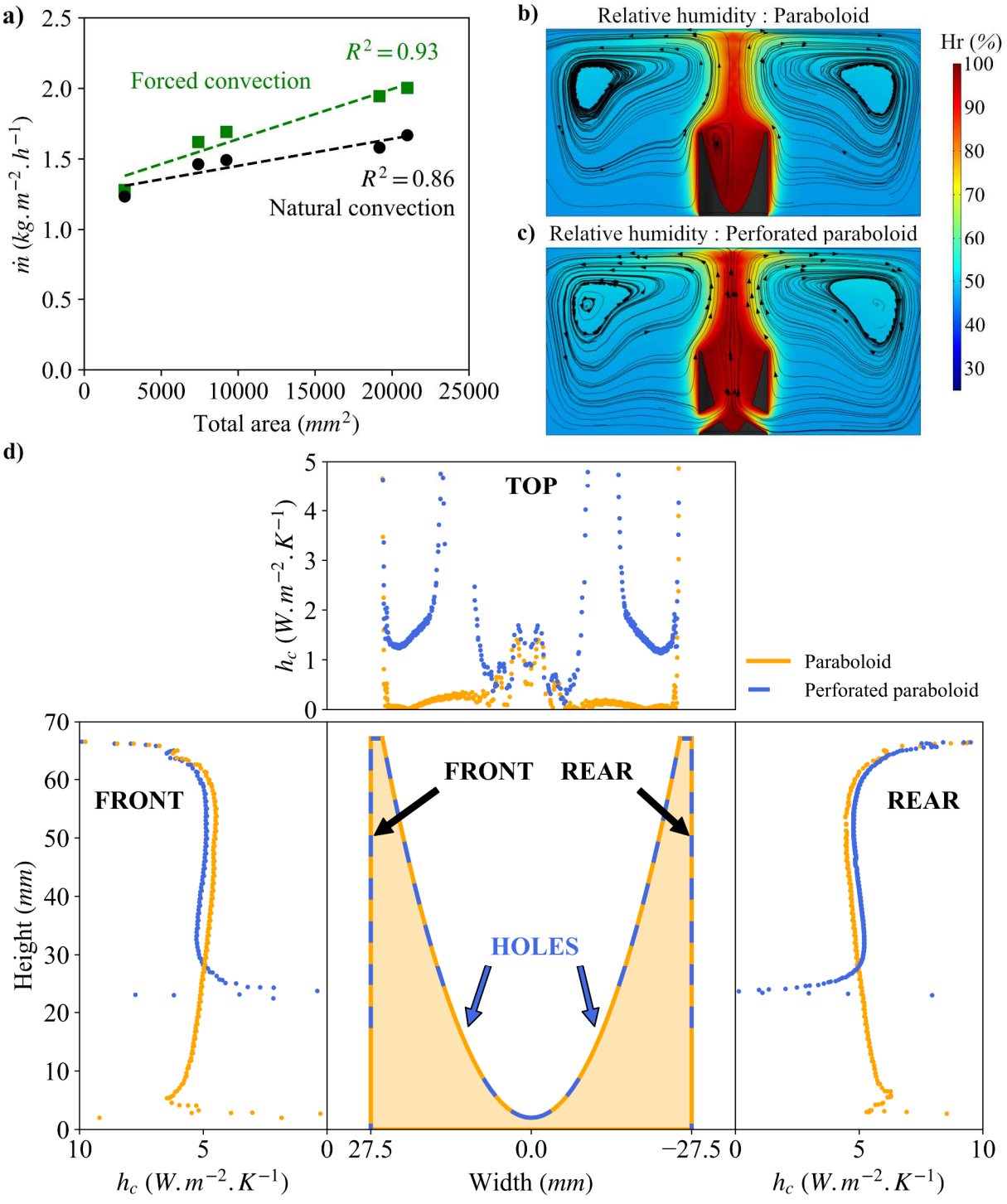

Fig. 9. a) Simulated evaporation rate for forced and natural convection for all geometries; relative humidity distribution and air flow velocity streamlines for the: b) paraboloid, and c) perforated paraboloid; d) heat transfer coefficients for the paraboloid (orange) and the perforated paraboloid (blue) under natural convection.

5 Conclusion

In this study, a novel solar evaporator combining a 3D-printed skeleton to create unique geometries and activated carbon (AC) to allow high photothermal properties and high evaporation rate was designed, modelled and validated using a set of experimental results obtained on different 3D evaporator geometries. An evaporation rate of 1.91 kg m^{-2} h^{-1} was achieved at 20°C under 1 sun illumination, using a paraboloid geometry with holes made at the bottom to allow air to pass from the bottom to the top to recycle water vapour-saturated air. It was found that the evaporation rate is highly dependent on the amount of surface area allowed to evaporate. Besides, the effect of surface-to-surface radiation in a concavity, a phenomenon assumed to increase evaporation, was found to have a limited impact on performance (1%) with the numerical approach. It was also found that the geometry used for evaporation must allow air to pass through, so that heat exchange is promoted by the airflow and water-saturated air can be evacuated, which was facilitated by the creation of two holes on the base of the 3D-printed paraboloid structure. Indeed, much of the performance was due to evaporation on the sides of the geometries, where the air circulated, while the top surface was more for solar concentration. This is also true for natural convection, where the flow is directed upwards, as the perforated geometry has been shown to exchange more in its concavity. In view of all these results, 3D structures should avoid concavity, as the impact of reflection is very limited compared to the local humidity saturation effect that limits concavity performance. Instead, 3D geometries should be as open as possible, to allow maximum evaporation area, not only to evaporate but also transport saturated air. With this new 3D-printed structure filled with AC, a wide variety of precise and open geometries can be achieved to further improve solar evaporation results under convective flow. Finally, the model can be refined to optimise the 3D-printed geometry to maximise airflow and create viable and efficient water evaporators. At present, the material is not optimized for seawater

519 conditions (Fig. S1). Further work will be needed on its ability to evacuate salt from the
520 exchange surface or to direct it to specific zones for recovery.

521 **Acknowledgements**

522 This work was supported by the French Ministry of the Armed Forces - Defence
523 Innovation Agency.

524 **References**

525 [1] G. Howard, J. Bartram, A. Williams, A. Overbo, D. Fuente, J.-A. GeereFor, Domestic
526 water quantity, service level and health, WHO, 2020. https://www.who.int/publications-
527 detail-redirect/9789240015241.

528 [2] C. Chen, Y. Kuang, L. Hu, Challenges and Opportunities for Solar Evaporation, Joule. 3
529 (2019) 683–718. https://doi.org/10.1016/j.joule.2018.12.023.

530 [3] N.S. Lewis, D.G. Nocera, Powering the planet: Chemical challenges in solar energy
531 utilization, Proc. Natl. Acad. Sci. U. S. A. 103 (2006) 15729–15735.
532 https://doi.org/10.1073/pnas.0603395103.

533 [4] R. Fillet, V. Nicolas, V. Fierro, A. Celzard, A review of natural materials for solar
534 evaporation, Sol. Energy Mater. Sol. Cells. 219 (2021) 110814.
535 https://doi.org/10.1016/j.solmat.2020.110814.

536 [5] G. Liu, T. Chen, J. Xu, G. Li, K. Wang, Solar evaporation for simultaneous steam and
537 power generation, J. Mater. Chem. A. 8 (2020) 513–531.
538 https://doi.org/10.1039/C9TA12211G.

539 [6] R. Fillet, V. Nicolas, V. Fierro, A. Celzard, Modelling heat and mass transfer in solar
540 evaporation systems, Int. J. Heat Mass Transf. 181 (2021) 121852.
541 https://doi.org/10.1016/j.ijheatmasstransfer.2021.121852.

542 [7] P. Zhang, Q. Liao, H. Yao, Y. Huang, H. Cheng, L. Qu, Direct solar steam generation
543 system for clean water production, Energy Storage Mater. 18 (2019) 429–446.
544 https://doi.org/10.1016/j.ensm.2018.10.006.

545 [8] G. Liu, J. Xu, K. Wang, Solar water evaporation by black photothermal sheets, Nano
546 Energy. 41 (2017) 269–284. https://doi.org/10.1016/j.nanoen.2017.09.005.

547 [9] X. Wu, G.Y. Chen, G. Owens, D. Chu, H. Xu, Photothermal materials: A key platform
548 enabling highly efficient water evaporation driven by solar energy, Mater. Today
549 Energy. 12 (2019) 277–296. https://doi.org/10.1016/j.mtener.2019.02.001.

550 [10] C. Xiao, S. Wang, Y. Guo, Y. Zhang, Q.-M. Hasi, Q. Tian, L. Chen, Coffee Grounds-
551 Doped Alginate Porous Materials for Efficient Solar Steam Generation, Langmuir. 38
552 (2022) 1888–1896. https://doi.org/10.1021/acs.langmuir.1c03102.

553 [11] H. Xie, W.-H. Xu, Y. Du, J. Gong, R. Niu, T. Wu, J.-P. Qu, Cost-Effective Fabrication
554 of Micro-Nanostructured Superhydrophobic Polyethylene/Graphene Foam with Self-
555 Floating, Optical Trapping, Acid-/Alkali Resistance for Efficient Photothermal Deicing

and Interfacial Evaporation, Small. 18 (2022) 2200175. https://doi.org/10.1002/smll.202200175.

[12] Y. Li, L. Xu, J. Cai, J. Liu, B. Lv, J. Chao, Q. Zhang, Y. Zhao, A Stable Bilayer Polypyrrole-Sorghum Straw Evaporator for Efficient Solar Steam Generation and Desalination, Adv. Sustain. Syst. 6 (2022) 2100342. https://doi.org/10.1002/adsu.202100342.

[13] C. Li, S. Cao, J. Lutzki, J. Yang, T. Konegger, F. Kleitz, A. Thomas, A Covalent Organic Framework/Graphene Dual-Region Hydrogel for Enhanced Solar-Driven Water Generation, J. Am. Chem. Soc. 144 (2022) 3083–3090. https://doi.org/10.1021/jacs.1c11689.

[14] M. Zhu, X. Liu, Y. Tian, A. Caratenuto, F. Chen, Y. Zheng, Dome-arrayed chitosan/PVA hydrogel-based solar evaporator for steam generation, Sci. Rep. 12 (2022) 4403. https://doi.org/10.1038/s41598-022-08589-z.

[15] Y. Wang, X. Wu, T. Gao, Y. Lu, X. Yang, G.Y. Chen, G. Owens, H. Xu, Same materials, bigger output: A reversibly transformable 2D–3D photothermal evaporator for highly efficient solar steam generation, Nano Energy. 79 (2021) 105477. https://doi.org/10.1016/j.nanoen.2020.105477.

[16] X. Liu, Z. Liu, D. Devadutta Mishra, Z. Chen, J. Zhao, C. Hu, Evaporation rate far beyond the input solar energy limit enabled by introducing convective flow, Chem. Eng. J. 429 (2022) 132335. https://doi.org/10.1016/j.cej.2021.132335.

[17] C. Ma, Q. Liu, Q. Peng, G. Yang, M. Jiang, L. Zong, J. Zhang, Biomimetic Hybridization of Janus-like Graphene Oxide into Hierarchical Porous Hydrogels for Improved Mechanical Properties and Efficient Solar Desalination Devices, ACS Nano. 15 (2021) 19877–19887. https://doi.org/10.1021/acsnano.1c07391.

[18] L. Peng, X. Gu, H. Yang, D. Zheng, P. Wang, H. Cui, Ultra-high evaporation rate 3D evaporator with vertical sheets based on full use of convection flow, J. Clean. Prod. 345 (2022) 131172. https://doi.org/10.1016/j.jclepro.2022.131172.

[19] M. Javed, S. Pirah, Y. Xiao, Y. Sun, Y. Ji, M.Z. Nawaz, Z. Cai, B. Xu, Complete System to Generate Clean Water from a Contaminated Water Body by a Handmade Flower-like Light Absorber, ACS Omega. 6 (2021) 35104–35111. https://doi.org/10.1021/acsomega.1c05925.

[20] M.-Y. Yu, C. Li, W. Li, P. Min, Reduced Graphene Oxide Decorated Cellulose Acetate Filter Evaporators for Highly Efficient Water Evaporation and Purification Driven by Solar Energy and Environmental Energy, Adv. Sustain. Syst. 6 (2022) 2200023. https://doi.org/10.1002/adsu.202200023.

[21] Md.N.A.S. Ivan, A.M. Saleque, S. Ahmed, P.K. Cheng, J. Qiao, T.I. Alam, Y.H. Tsang, Waste Egg Tray and Toner-Derived Highly Efficient 3D Solar Evaporator for Freshwater Generation, ACS Appl. Mater. Interfaces. 14 (2022) 7936–7948. https://doi.org/10.1021/acsami.1c22215.

[22] L. Li, K. Chen, J. Zhang, Superelastic Clay/Silicone Composite Sponges and Their Applications for Oil/Water Separation and Solar Interfacial Evaporation, Langmuir. 38 (2022) 1853–1859. https://doi.org/10.1021/acs.langmuir.1c03043.

[23] Q. Zhang, L. Ren, X. Xiao, Y. Chen, L. Xia, G. Zhao, H. Yang, X. Wang, W. Xu, Vertically aligned Juncus effusus fibril composites for omnidirectional solar evaporation, Carbon. 156 (2020) 225–233. https://doi.org/10.1016/j.carbon.2019.09.067.

[24] W. Guan, Y. Guo, G. Yu, Carbon Materials for Solar Water Evaporation and Desalination, Small. 17 (2021) 2007176. https://doi.org/10.1002/smll.202007176.

[25] S.K. Hota, G. Diaz, Enhancing solar water evaporation with activated carbon, MRS Adv. 5 (2020) 2565–2574. https://doi.org/10.1557/adv.2020.267.

[26] N. Arshad, I. Ahmed, M.S. Irshad, H.R. Li, X. Wang, S. Ahmad, M. Sharaf, M. Firdausi, M. Zaindin, M. Atif, Super Hydrophilic Activated Carbon Decorated Nanopolymer Foam for Scalable, Energy Efficient Photothermal Steam Generation, as an Effective Desalination System, Nanomaterials. 10 (2020) 2510. https://doi.org/10.3390/nano10122510.

[27] A. Mnoyan, M. Choi, D.H. Kim, B.-J. Ku, H. Kim, K.J. Lee, A.S. Yasin, S. Nam, K. Lee, Cheap, facile, and upscalable activated carbon-based photothermal layers for solar steam generation, RSC Adv. 10 (2020) 42432–42440. https://doi.org/10.1039/D0RA07746A.

[28] X. Zhao, Y. Chen, Y. Yin, L. Zou, Q. Chen, K. Liu, P. Lin, H. Su, Y. Chen, Janus Polypyrrole Nanobelt@Polyvinyl Alcohol Hydrogel Evaporator for Robust Solar-Thermal Seawater Desalination and Sewage Purification, ACS Appl. Mater. Interfaces. 13 (2021) 46717–46726. https://doi.org/10.1021/acsami.1c13584.

[29] Y. Shi, R. Li, Y. Jin, S. Zhuo, L. Shi, J. Chang, S. Hong, K.-C. Ng, P. Wang, A 3D Photothermal Structure toward Improved Energy Efficiency in Solar Steam Generation, Joule. 2 (2018) 1171–1186. https://doi.org/10.1016/j.joule.2018.03.013.

[30] Y. Yang, W. Fan, S. Yuan, J. Tian, G. Chao, T. Liu, A 3D-printed integrated MXene-based evaporator with a vertical array structure for salt-resistant solar desalination, J. Mater. Chem. A. 9 (2021) 23968–23976. https://doi.org/10.1039/D1TA07225K.

[31] X. Zhang, L. Ren, J. Xu, B. Shang, X. Liu, W. Xu, Magnetically Driven Tunable 3D Structured Fe3O4 Vertical Array for High-Performance Solar Steam Generation, Small. 18 (2022) 2105198. https://doi.org/10.1002/smll.202105198.

[32] V. Nicolas, F. Vanin, D. Grenier, T. Lucas, C. Doursat, D. Flick, Modeling bread baking with focus on overall deformation and local porosity evolution, AIChE J. 62 (2016) 3847–3863. https://doi.org/10.1002/aic.15301.

[33] H. Song, Y. Liu, Z. Liu, M.H. Singer, C. Li, A.R. Cheney, D. Ji, L. Zhou, N. Zhang, X. Zeng, Z. Bei, Z. Yu, S. Jiang, Q. Gan, Cold Vapor Generation beyond the Input Solar Energy Limit, Adv. Sci. 5 (2018) 1800222. https://doi.org/10.1002/advs.201800222.

[34] S. Li, Y. He, Y. Wang, D. Liao, H. Liu, L. Zhou, C. Wei, C. Yu, Y. Chen, Simple Hierarchical Interface Design Strategy for Accelerating Solar Evaporation, Macromol. Mater. Eng. n/a (n.d.) 2000640. https://doi.org/10.1002/mame.202000640.

[35] T. Gao, X. Wu, Y. Wang, G. Owens, H. Xu, A Hollow and Compressible 3D Photothermal Evaporator for Highly Efficient Solar Steam Generation without Energy Loss, Sol. RRL. 5 (2021) 2100053. https://doi.org/10.1002/solr.202100053.

[36] C. Kim, D. Shin, M.N. Baitha, Y. Ryu, A.M. Urbas, W. Park, K. Kim, High-Efficiency Solar Vapor Generation Boosted by a Solar-Induced Updraft with Biomimetic 3D Structures, ACS Appl. Mater. Interfaces. 13 (2021) 29602–29611. https://doi.org/10.1021/acsami.1c05883.